Heat Budget in the Kuroshio Extension Region: 1993–99

FRÉDÉRIC VIVIER*

Applied Physics Laboratory, School of Oceanography, University of Washington, Seattle, Washington

KATHRYN A. KELLY

Applied Physics Laboratory, University of Washington, Seattle, Washington

LUANNE THOMPSON

School of Oceanography, University of Washington, Seattle, Washington

(Manuscript received 11 July 2001, in final form 21 May 2002)

ABSTRACT

Processes responsible for the seasonal and interannual variations of the sea surface temperature as well as of the heat content of the upper ocean (0–400 m) in the Kuroshio Extension region are examined from a 3D advection–diffusion model in finite elements, with an embedded bulk mixed layer. The geostrophic velocity is specified externally from TOPEX/Poseidon altimeter data, and Ekman velocity is specified from NCEP wind stress. The thermal field from the model shows good agreement with observations. While both atmospheric and oceanic processes are required to explain observed nonseasonal SST changes, the interannual heat storage rate is dominated by horizontal advection. In particular, the transition between an elongated and a contracted state of the Kuroshio caused by geostrophic advection has a clear signature in the SST. There is an indication that this process is accompanied by consistent changes in nonseasonal entrainment: when the Kuroshio is in an elongated state and warmer waters are present below the mixed layer, entrainment appears less efficient in exporting heat out of the mixed layer.

1. Introduction

The North Pacific climate system has recently been found to have important interannual-to-decadal fluctuations (e.g., Trenberth and Hurrel 1994), with a remarkable transition in the late 1970s, revealed for instance in the sea surface temperature (SST; Fig. 1). This variability of the ocean–atmosphere system, with important climatic consequences and direct economic impact over North America, has been termed the Pacific decadal oscillation (PDO; Mantua et al. 1997). It is not clear whether the PDO is driven by decadal changes in the Tropics through atmospheric teleconnection (e.g., Zhang et al. 1997), or whether the driving mechanism is confined to the midlatitude, acting independently of the Tropics. In the latter case, decadal variability could result from an active ocean–atmosphere coupling (Latif and Barnett 1994; Jin 1997) or alternatively from a passive ocean response to stochastic forcing from the atmosphere (Frankignoul et al. 1997).

In any event, the region of the Kuroshio Extension (hereafter KE) plays a distinctive and important role. With warm subtropical waters being advected into contact with cold air masses, it is the region where heat exchanges between the ocean and atmosphere are largest in the extratropical North Pacific, and therefore where the ocean may most actively influence the atmosphere on a wide range of timescales. In particular, on interannual to decadal timescales, this region has the largest variability over the North Pacific both in SST and subsurface temperature (Miller et al. 1998; Xie et al. 2000). Both modeling and observations suggest that changes in the subsurface thermal field are primarily caused by changes in the wind-driven circulation consistent with Sverdrup theory (Miller et al. 1998; Deser et al. 1999). In addition Schneider et al. (2002) find that Rossby waves excited in the interior midlatitude Pacific by the wind ultimately modify the currents and subsurface temperature field of the KE region, generating SST anomalies. This mechanism shows skill in predicting wintertime SST up to three years in advance (Schneider and Miller 2001). Figure 1 suggests that substantial inter-

* Current affiliation: Laboratoire d'Océanographie Dynamique et de Climatologie, Université Pierre et Marie Curie, Paris, France.

Corresponding author address: Dr. Frédéric Vivier, LODYC, Tour 15, étage 2, Université P. et M. Curie, 4, place Jussieu, 75252 Paris, Cedex 05, France.
E-mail: fvi@lodyc.jussieu.fr

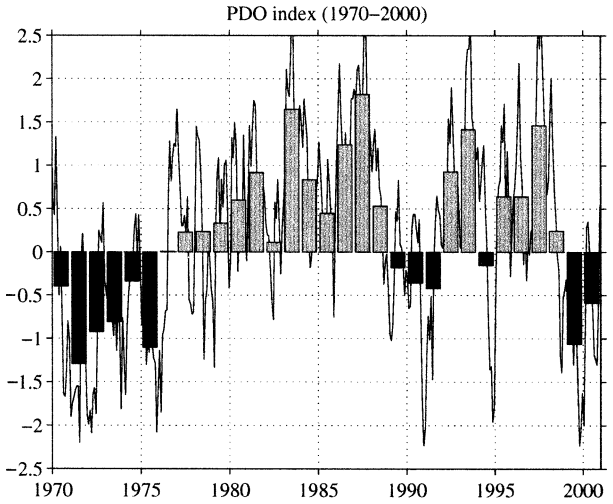

FIG. 1. PDO index derived from the leading principal component of the SST anomaly in the North Pacific (courtesy of N. Mantua). Bars indicate annual mean. A positive index (''warm'' PDO phase) is associated with a cold SST anomaly in the Kuroshio region, and vice versa.

annual changes in the SST field have occurred during the last decade over the KE, with an indication of a regime shift after 1999 (that also happens to correspond to a major El Niño to La Niña transition).

Understanding these recent strong signals in the dynamical and thermodynamical properties of the KE and its recirculation gyre appear important in the context of the PDO. These were recently documented by Qiu (2000), who analyzed the variations of the sea surface height (SSH) from the first seven years of the TOPEX/Poseidon (T/P) mission. He showed that the KE oscillates between an elongated state (characterized by larger eastward surface transport, greater zonal penetration, and a path shifted to the north) and a contracted state. Concomitant changes are observed in the southern recirculation gyre, which is larger (weaker) in elongated (contracted) phases. In addition, Qiu (2000) found that these large-scale interannual changes have a significant impact (>1°C) on the regional wintertime SST anomaly: positive (negative) for the elongated (contracted) state and the result of anomalous geostrophic advection.

In the present study, we elaborate on Qiu's work by investigating both the heat budget of the upper ocean (0–400 m) and the SST tendency balance between 1993 and 1999, using an advective ocean model with an embedded mixed layer. The North Pacific Ocean was previously studied by Auad et al. (1998) who used a primitive equation model, but did not detail the heat budget in the Kuroshio region. Here, rather than taking a purely numerical approach, we rely on altimeter data to determine geostrophic advection, following several previous studies (Qiu and Kelly 1993; Kelly and Qiu 1995a,b). Significant extensions are nevertheless made, the most important being that the model is three-dimensional and permits exchanges of heat between the mixed layer (ML) and the thermocline. This enables us, provided acceptable agreement with observations is reached, to detail the contribution of the different terms of the heat budget, as well as the vertical distribution of heat throughout the water column. In particular, we will address the following questions: Which mechanism has the largest impact on interannual SST changes? What causes the observed interannual fluctuations of heat content of the upper ocean?

For the mixed layer in our model we used a bulk formula, which is an efficient alternative to more sophisticated layered models that require a few parameters to be tuned against observations (Gaspar 1988). Among these, the temperature jump at the base of the ML, which directly affects its deepening rate, is perhaps the most arbitrary, since it depends on the previous cycle of entrainment and detrainment, as well as advection below the ML, which cannot be ignored in western boundary currents. This prompted us to couple the ML model to an advective–diffusive (AD) model of the temperature field of the upper ocean, developed in finite elements. The coupling is achieved by modifying the thermal field of the ocean model such that integral properties (heat content or potential energy) of the water column are conserved (Adamec et al. 1981). This technique of embedding has been used in several recent studies to retain the evolution of the stratification (e.g., Battisti et al. 1995; Alexander et al. 2000), although in these studies the ocean model is motionless and there is no connection between neighboring water columns. Here we have included in the three-dimensional model the processes of Ekman and geostrophic advection, and vertical Ekman pumping. We neglect salinity as this field cannot be adequately specified at the model boundaries due to the lack of repeat observations.

This study is organized as follows. The model is described in section 2; the seasonal and interannual variations of the ML depth, ML temperature, and heat content are compared with observations and analyzed in section 3; the heat budgets, both for the ML and the water column (down to 400 m), are discussed in section 4. A discussion of these results is presented in section 5.

2. Model

a. Advection–diffusion model

1) FORMULATION

The AD model includes a single equation for the temperature T:

$$\frac{\partial T}{\partial t} + (\mathbf{u}_g + \mathbf{u}_{\mathrm{Ek}}) \cdot \boldsymbol{\nabla} T + w\frac{\partial T}{\partial z} = \kappa_h \nabla^2 T + \kappa_v \frac{\partial^2 T}{\partial z^2} - \frac{1}{\rho_0 c_p}\frac{dq}{dz}, \qquad (1)$$

where $\mathbf{u}_g$, $\mathbf{u}_{\mathrm{Ek}}$, and w are the geostrophic, Ekman, and vertical velocity, respectively, all of which are time

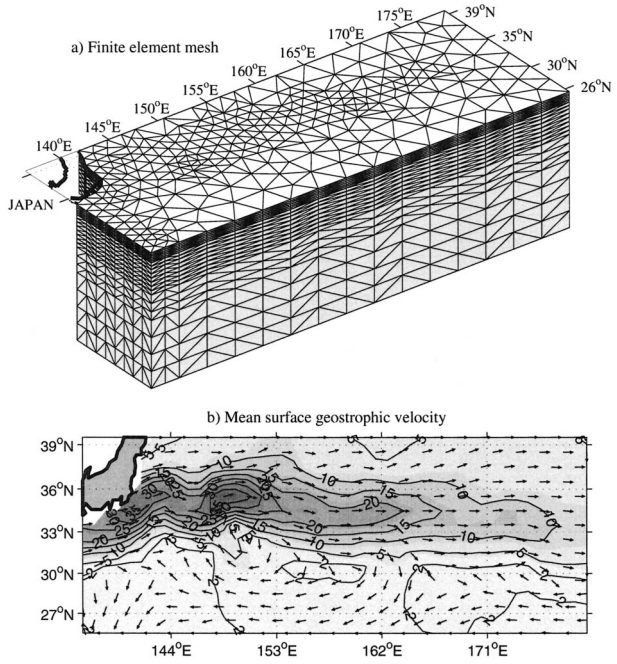

FIG. 2. Model mesh and mean surface geostrophic velocity. (a) View of the mesh of the model: horizontal levels (ranging from the surface down to 800 m) are mapped by triangular elements; nodes at each level are then connected to their counterparts in adjacent levels to form prismatic elements, each being in turn divided into three tetrahedrons. The horizontal resolution of the mesh is ~200 km, refined to ≲100 km in areas of important SSH gradients and near the western boundary. (b) Mean geostrophic velocity obtained from the mean SSH derived by Qiu (1995). Arrows have unit length and indicate direction only, whereas the modulus is contoured (cm s^{-1}).

varying fields specified externally (section 2). Parameters κ_h and κ_v are the horizontal and vertical temperature diffusivity; ρ_0 and c_p are the density and specific heat at constant pressure of seawater, respectively; and q is the radiative heating. Solar radiation absorption is given by

$$q(z) = q(0) \times [R \exp(z/\gamma_1) + (1 - R) \exp(z/\gamma_2)], \quad (2)$$

where, R, γ_1, and γ_2 parameterize the absorption properties of the water (Paulson and Simpson 1977). Two different parameterizations have subsequently been tested (section 3): waters of type 2 ($R = 0.77$, $\gamma_1 = 1.5$ m, $\gamma_2 = 14.0$ m) and waters of type 1a ($R = 0.62$, $\gamma_1 = 0.6$ m, $\gamma_2 = 20.0$ m). While the choice of a specific parameterization has little effect in winter when the ML is deep, it is critical for shallow summer ML since it determines the proportion of radiative heating escaping the ML and directly warming the seasonal thermocline.

The domain of study ranges from 25° to 40°N, from 136°E to 180°, and from the surface down to 800 m. In the horizontal, the domain is discretized with triangular elements (Fig. 2a). The horizontal resolution is typically ~200 km, but the mesh has been refined (≲100 km) in the Kuroshio pathway. The model includes 21 vertical levels unevenly spaced (15 of which are above 300 m). The volume is then entirely discretized in tetrahedrons, connecting the triangular mesh at each vertical level. The variational form of (1) is derived, and a piecewise linear solution is calculated (e.g., Rao 1989). The time scheme is Euler implicit, with a time step of ~12 h, satisfying the Courant–Friedrichs–Lewy (CFL) condition for the horizontal resolution of the mesh.

Boundary conditions are of two types: 1) T is specified at inflow regions (western, northern, and southern boundaries, the latter two being important for inflow by predominantly meridional Ekman currents) as well as at the bottom, and 2) with zero heat flux ($\partial T/\partial n = 0$) at the eastern boundary. The temperature field is from the Joint Environmental Data Analysis Center (JEDAC) database, derived from XBT data, down to 400 m. The temperature field is therefore completed from 400 to 800 m using climatology [*World Ocean Atlas 98* (*WOA98*); Antonov et al. 1998]. Note that the model carries interannual thermal variations in the upper 400 m only.

2) SPECIFICATION OF THE 3D VELOCITY FIELD

The horizontal velocity field includes both Ekman and geostrophic components. Geostrophic velocity at the surface is derived from 10-day SSH maps of T/P altimeter data, as in Qiu and Kelly (1993). In this dataset, the SSH field is the anomaly relative to an unknown mean sea level. The latter has been reconstructed with a 1° resolution by Qiu (1995), combining 1992–98 T/P data processed according to the synthetic jet method (Kelly and Gille 1990; Qiu et al. 1991) with hydrographic data. The mean geostrophic velocity is shown in Fig. 2b. A diagnostic analysis of the mean heat budget based on observed temperature (from Reynolds and Smith 1994) suggests that the mean velocity field may be modified to correct for local imbalances and capture part of the residual of the heat balance. Although heat budget imbalances seem for the most part to reflect a mismatch in the resolution of the SSH and SST fields, a correction to the mean SSH field obtained from the residual is proposed in appendix A, and has been applied thereafter.

The horizontal velocity field at successive depths is derived from the surface field after accounting for the vertical geostrophic velocity shear. Although the most legitimate approach would be to estimate the velocity shear based on the actual density field from the model, the neglect of salinity in the model prevented this, and the shear was instead estimated from climatology. Calculations made with the *WOA98* climatology throughout the domain suggest that the vertical velocity shear presents a relatively small seasonal cycle, and can be taken as constant with time as a first approximation. From this dataset it also appears that there is little rotation of the velocity field with depth. Rotation effects are therefore ignored and the vertical shear is applied in the plane

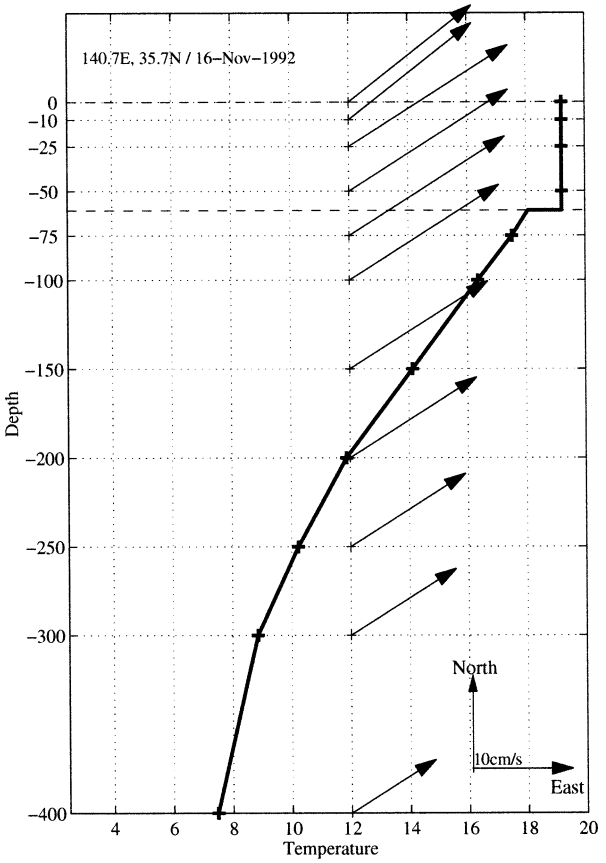

FIG. 3. Example of a vertical profile of temperature and horizontal velocity (geostrophic plus Ekman) at 36°N and 141°E in Nov 1992. Profiles are piecewise linear and discontinuous at the base of the ML. For practical reasons, Ekman flow is supposed to be carried entirely in the first layer; horizontal velocity is therefore constant in the ML only starting at the third level.

defined by the surface velocity vector (the ''reference'' velocity derived from altimeter data) and the vertical direction (Fig. 3). Although the approximations made here are quite crude, we note that most significant discrepancies between the altimeter-derived velocity field and the thermal wind field occur at places where the magnitude of the velocity is small, therefore with presumably a limited impact on the heat budget.

Added to the geostrophic field, the Ekman transport is obtained from the surface wind stress τ according to $\mathbf{U}_{\mathrm{Ek}} = \tau/\rho_0 f \times \mathbf{k}$, where f is the Coriolis parameter and $\mathbf{k}$ is the vertical unit vector. The Ekman transport is assumed to be confined to the uppermost layer (0–10 m), so as to always lie within the ML (Fig. 3). Since the ML temperature is vertically homogenized after the advection time step, this scheme is equivalent to assuming Ekman transport to be homogeneously distributed over the entire ML, as in Frankignoul (1985).

The time-varying vertical velocity is taken constant with depth and equal to the Ekman pumping velocity, $w(x, y) = \boldsymbol{\nabla}\cdot\mathbf{U}_{\mathrm{Ek}} = \mathrm{curl}(\tau/\rho_0 f)$, except for the first layer where it linearly goes to zero at the surface.

3) ADVECTION OF THE MIXED LAYER INTERFACE

At each time step, prior to considering changes caused by turbulent processes, the ML depth h is advected (and diffused) as a material surface by the flow according to $\partial_t h + \boldsymbol{\nabla}\cdot\mathbf{U} = \kappa_H \nabla^2 h$, where $\mathbf{U}$ is the total horizontal transport integrated over the depth of the ML. This equation is solved on the bidimensional mesh of triangular elements. The ML depth h is specified at the same lateral boundaries as for the temperature field from the JEDAC dataset based on

$$\int_{-h}^{0} T(z)\, dz - T(-h) = 1^{\circ}\mathrm{C}. \tag{3}$$

b. Mixed layer model

1) MIXED LAYER DEPTH

Changes in ML depth are based on the budget of turbulent kinetic energy (TKE). When TKE is available for deepening, the ML entrains waters from below at a rate defining the entrainment velocity w_e (i.e., $\partial_t h = w_e$ for $\partial_t h > 0$, otherwise $w_e = 0$). Ignoring the effect of salinity on buoyancy, w_e is determined from the parameterization of Niiler and Kraus (1977) according to

$$\frac{1}{2}\alpha g \Delta T w_e = (m_2 + m_3)u_*^3 - \frac{1}{2}hB(h) - h\epsilon_m, \tag{4}$$

where α is the thermal expansion coefficient, g is the gravitational acceleration, ΔT is the discontinuity of temperature across the base of the ML, $u_* = \sqrt{\|\tau\|/\rho_0}$ is the frictional velocity, m_i are scalar parameters, ϵ_m parameterizes dissipation terms, and the buoyancy forcing term $B(h)$ is given by

$$B(h) = \frac{\alpha g}{\rho_0 c_p}\left[Q_{\mathrm{net}} + q(-h) - \frac{2}{h}\int_{-h}^{0} q(z)\, dz\right]. \tag{5}$$

Here, Q_{net} is the net heat flux from the atmosphere to the ocean at the surface (incoming shortwave and outgoing infrared radiation, latent and sensible heat fluxes), and the downward radiation $q(z)$ has been defined in (2).

The parameterization of turbulent dissipation is generally what differentiates the different bulk ML models. We adopt here the formulation of Gaspar (1988), which has been developed for long-term simulations, keeping his calibration for the tunable parameters. When the ML shallows, h is no longer a prognostic quantity, but is instead determined diagnostically assuming a balance between TKE production and dissipation, which in the formulation of Gaspar yields

$$\mathrm{cp}_3 u_*^3 - \mathrm{cp}_1 hB(h) = 0, \tag{6}$$

where parameters cp_3 and cp_1, defined in his Eq. (50), depend both on the Monin–Obukhov length scale $[u_*^3/B(h)]$ and the Ekman length scale (u_*/f). Following

Battisti et al. (1995), the retreat depth is determined by iterative resolution of (6), but the ML is forced to remain deeper than the first vertical grid point (10 m).

2) MIXED LAYER TEMPERATURE

Assuming the entrainment rate and ΔT to be known, vertical integration of the heat equation yields a prognostic equation for the ML temperature:

$$h\frac{\partial T_m}{\partial t} = \frac{Q_{\text{net}} - q(-h)}{\rho_0 c_p} - w_e \Delta T - \kappa_v \frac{\partial \overline{T}}{\partial z}(-h), \quad (7)$$

where there is no heat exchange with underlying layers during detrainment (i.e., $w_e = 0$).

3) COUPLING TO THE ADVECTION–DIFFUSION MODEL

The vertical resolution of the AD model is too coarse to permit a simple insertion of T_m over the depth h determined from the ML model. Instead, the ML is embedded into the 3D grid as by Adamec et al. (1981), with some adjustments to account for the finite element mesh. The general principle of the coupling method, described in more detail in appendix B, is to carry and store at each time step two additional fields, beside the 3D temperature field: the ML depth and the temperature at the base of the ML. Prior to the advection diffusion step by the 3D velocity field, vertical temperature profiles, which are by essence discontinuous at the base of the ML, are changed to piecewise linear profiles in such a way that the heat content of the water column is preserved. After the temperature field has been advected, the discontinuity at the base of the ML is restored (still conserving heat) before consideration of turbulent processes affecting the ML (causing entrainment or detrainment).

c. Model parameters and forcing fields

Model parameters are $\kappa_h = 3000$ m^2 s^{-1} for the horizontal diffusivity of temperature, chosen to agree with the estimate of Ostrovskii and Piterbarg (2000) in the Kuroshio region, whereas vertical diffusivity is $\kappa_v = 2 \times 10^{-5}$ m^2 s^{-1}.

The model is run from October 1992 to March 2000 (T/P period). It is initialized with JEDAC temperature data above 400 m and *WOA98* data below. SSH data from T/P are used to derive the geostrophic velocity, but also for comparison with heat content estimates from the model (section 3). These were mapped onto a regular grid by staff at Oregon State University, who used the mapping method of Chelton and Schlax (1994) to minimize tidal aliasing (smoothed in space and time with half spans of 6° and 20 days, respectively).

The model is forced with several products derived from the National Centers for Environmental Prediction (NCEP) daily reanalyzed fields (Kalnay et al. 1996).

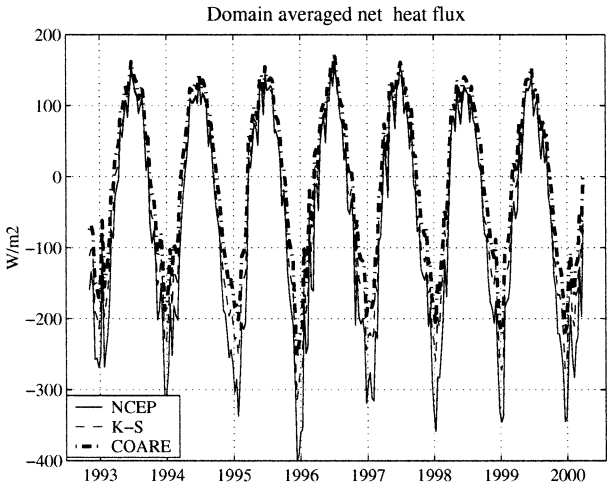

FIG. 4. Domain average of the net heat flux (radiative and turbulent) for three different parameterizations of the latent and sensible heat fluxes.

Problems have been reported with NCEP turbulent fluxes: the bulk flux algorithm was found inappropriate under moderate to strong wind conditions. Latent and sensible fluxes are overestimated by as much as 34% and 22%, respectively (the heat loss to the atmosphere is exagerated in NCEP), from the study of Zeng et al. (1998), and by 27% and 51% in the work of Renfrew et al. (2002). Thus, to correct for these biases as well as to test the sensitivity of the model to differences in the thermal forcing, we have derived two alternative products of turbulent heat fluxes using instead the TOGA COARE (Tropical Ocean and Global Atmosphere Coupled Ocean–Atmosphere Response Experiment) bulk algorithm version 2.5b (Fairall et al. 1996) on the one hand, and a hybrid parameterization based on Kondo (1975) (for low wind conditions) and Smith (1988) (for high winds), which is part of the University of Washington planetary boundary layer model (Brown and Liu 1982), denoted K–S hereafter, on the other hand. In these calculations, we have used NCEP fields for SST, winds, air temperature, and specific humidity. Only the algorithm to compute the fluxes is different. Although the same parameterization is used by NCEP for momentum fluxes, the discrepancy is found not to be as acute (Renfrew et al. 2002), and no correction is made here.

Figure 4 shows the domain average of the three turbulent heat flux estimates. Largest discrepancies occur during winter, when strong wind conditions are experienced, whereas summer estimates are fairly close. In the inflow region of the Kuroshio, K–S's parameterization leads to net heat losses (negative fluxes) to the atmosphere which are 36% smaller than NCEP in the annual mean, whereas estimates obtained with COARE are 64% smaller (a mean difference of 90 W m^{-2}).

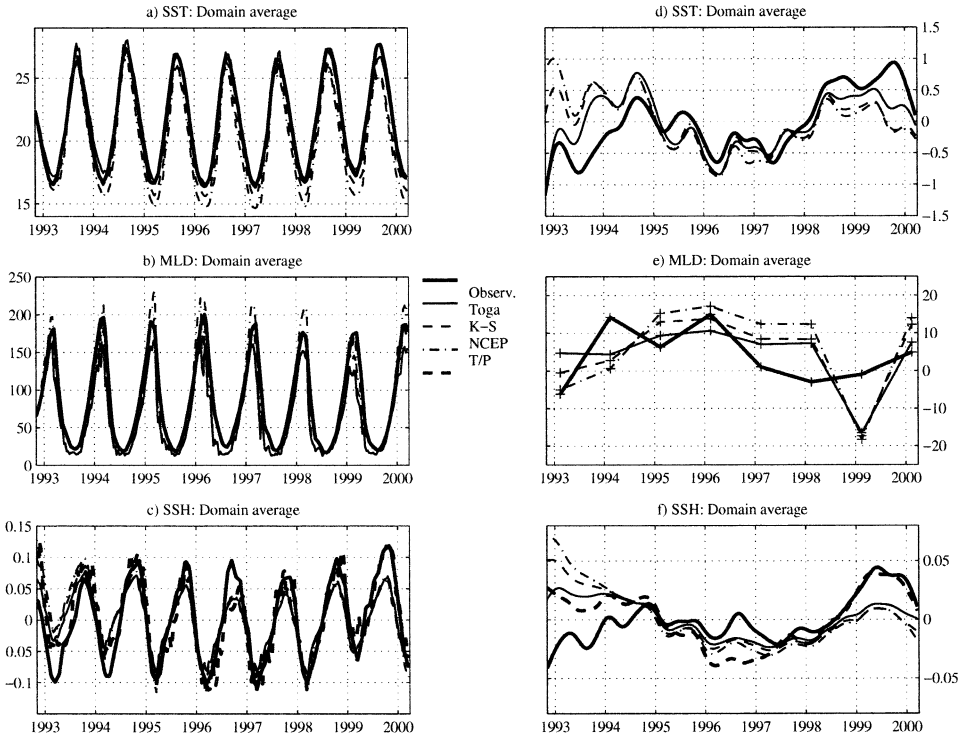

FIG. 5. Domain average of the ML temperature, MLD, and sea surface height anomaly: (a) SST (°C) from Reynolds (thick), from the model forced with NCEP fluxes (thin dash–dot), from the model forced with fluxes derived from the Kondo–Smith bulk algorithm (thin dashed), and from the model forced with fluxes derived from the TOGA COARE bulk algorithm (thin); (b) same as (a) but for the ML depth (m); (c) same as (a) but for the SSH (m), shown together with the SSH from T/P (thick-dashed). Right panels [(d)–(f)] are the anomalies from the monthly mean (series are low-pass filtered with a cutoff period at 250 days for clarity), except for MLD for which the anomaly relative to wintertime (JFM) averages is instead presented.

3. Comparison of model outputs with observations

We focus on two types of observations to assess the performance of the model: the ML temperature (compared with the SST from Reynolds and Smith 1994) on the one hand and the steric height change (compared with the SSH from T/P) on the other hand. In addition, the ML depth is compared with estimates derived from JEDAC temperature data according to (3).

The SSH is used as a proxy for the heat content of the water column (ignoring the barotropic contribution as well as salinity effects; see, e.g., Vivier et al. 1999). The steric height change η is derived from the temperature field of the model (assuming a salinity of 35) according to $\eta = 1/g \int_0^{400\text{dbar}} 1/\rho(35, T, p) - 1/\rho(35, 0, p)\, dp$, from which we remove the long-term mean (1992–2000) for comparison with T/P. The integral is carried out down to 400 m only because we impose climatological temperature at the boundaries below that depth. This is likely to affect the comparisons between the model SSH and the SSH from T/P, particularly on interannual time scales. However, most of the thermal expansion or contraction occurs in the uppermost fraction of the ocean, because of the sensitive dependence of the thermal expansion coefficient on temperature. In the Kuroshio region, a given positive heat flux will cause an expansion at 500 m, which is about half the one that the same flux would generate at the surface.

a. Influence of the heat flux product

Before examining the heat budget, we seek to determine which of the three heat flux products discussed in the previous section yields the closest agreement between model and observations. Three model runs were therefore performed, forced with NCEP, K–S, and COARE heat fluxes, respectively, and using waters of type 2 for the radiative heating (2). Three additional runs were carried out, assuming instead waters of type 1a, to allow more heat to escape the shallow ML in summer. This enabled us to select heat flux/water type combinations that best matched SST observations: NCEP/type 2, K–S/type 2, and COARE/type 1a, which are discussed in more detail now.

Figure 5a shows the domain average of the SST for each model run. Although the amplitude of the seasonal cycle is comparable to observations for each run, a long-term trend toward cooler temperature is apparent in the SST from the model forced with NCEP heat fluxes (Fig.

5a; thin dash–dot line), with temperatures more than 2°C cooler than observations after 2 years of integration. This failure to adequately close the heat budget on interannual time scales could be attributed to two main candidates: the region could cool off because advection of heat into the domain is underestimated, or alternatively, because heat losses to the atmosphere are overestimated. Without additional evidence that heat losses are overestimated by NCEP (Zeng et al. 1998; Renfrew et al. 2002) it would be difficult to select the cause. Kondo–Smith's parameterization yields a SST that does not present this interannual cooling, but it nevertheless fails to reproduce the long term warming trend apparent in observations (Fig. 5a; thin dashed line). It is with the TOGA COARE parameterization that observations of SST are best reproduced (Fig. 5a; thin line, hardly distinguishable from the thick line). On interannual timescales, COARE fluxes give a modeled SST closest to observations, with an acceptable representation of the warming trend (Fig. 5d, thin line).

The mixed layer depth (MLD) for the three runs of the model differ most noticeably in wintertime (Fig. 5b). While NCEP fluxes lead to an overestimated MLD, and COARE fluxes lead, conversely, to an underestimate, it is with K–S's parameterization that the closest agreement with observations is found. Anomalies of the mean wintertime (January–February–March, hereafter JFM) MLD are shown in Fig. 5e. Although interannual changes in the MLD are well reproduced in the upstream Kuroshio region (west of 155°E; not shown), the model MLD reproduces, only roughly, observations when averaged over the whole domain, with a deeper ML in 1995 and 1996, decreasing afterward. It differs most notably from observations in JFM 1999, with a sharp negative anomaly for all three runs. This anomaly is expected given the remarkably low winds during this winter (Fig. 6; top), resulting in both smaller wind stirring and heat loss to the atmosphere (Fig. 6; bottom), hence a shallower ML. MLD is derived from observations according to (3), which is a somewhat arbitrary criterion (section 3b; Fig. 8), suggesting that it should perhaps not be considered as accurate a measure of the performances of the model as SST itself is.

Finally, the SSH anomaly derived from the temperature field is compared with the SSH from T/P (Fig. 5c, thick dashed line). The agreement between the model and T/P is fairly good from 1992 to winter 1998/99 suggesting that the subsurface temperature field is adequately represented. The model reproduces acceptable interannual SSH variations up to 1999 (Fig. 5f). Surprisingly the agreement is even better than that between T/P and the SSH derived from JEDAC temperature observations up to 1998 (perhaps due to a poor subsurface sampling), except after 1998, where the agreement becomes excellent. It is interesting to note that the estimate of SSH anomaly from the model becomes relatively insensitive to the heat flux product being used after 1995, which suggests that horizontal advection of heat becomes an even more important contribution afterwards, or instead that Q_{net} does not dominate SSH.

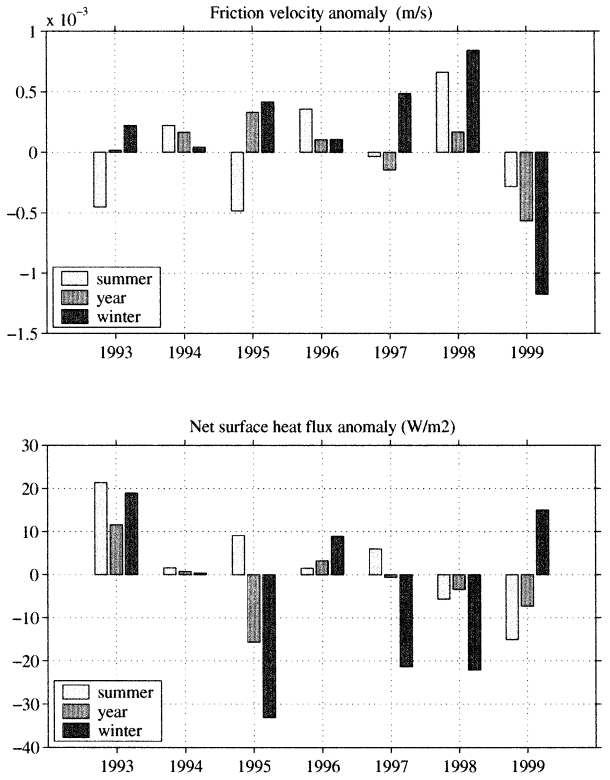

FIG. 6. (top) Nonseasonal friction velocity ($u_* = \sqrt{\|\boldsymbol{\tau}\|/\rho_0}$) and (bottom) net heat flux averaged over the domain. Anomalies are shown for summer months (Jul–Aug–Sep; light bars), winter months (JFM; black bars), and averaged over the whole year (gray bars).

From these comparisons we conclude that the model forced with TOGA COARE turbulent fluxes gives the best overall agreement with observations (it is the only run for which the warming trend in SST is reproduced), and therefore only this run is discussed in more detail hereafter. However, given the crude hypothesis made for estimating subsurface advection, it is not possible to assess unambiguously which of the heat flux products is the best; low values from TOGA COARE could simply be compensating for errors in the subsurface advection of heat. Radiative fluxes are another potential source of error, which influence has not been tested here. Scott and Alexander (1999) show biases of 20 W m^{-2} in summer between NCEP shortwave radiation and observations.

b. Model forced with COARE fluxes

1) SEASONAL VARIATIONS

Seasonal averages of the MLD, SST, and the SSH anomaly have been derived both for the model and for the observations between 1992 and 2000. These are used to assess the performance of the model forced with COARE fluxes for winter months (Fig. 7). Although

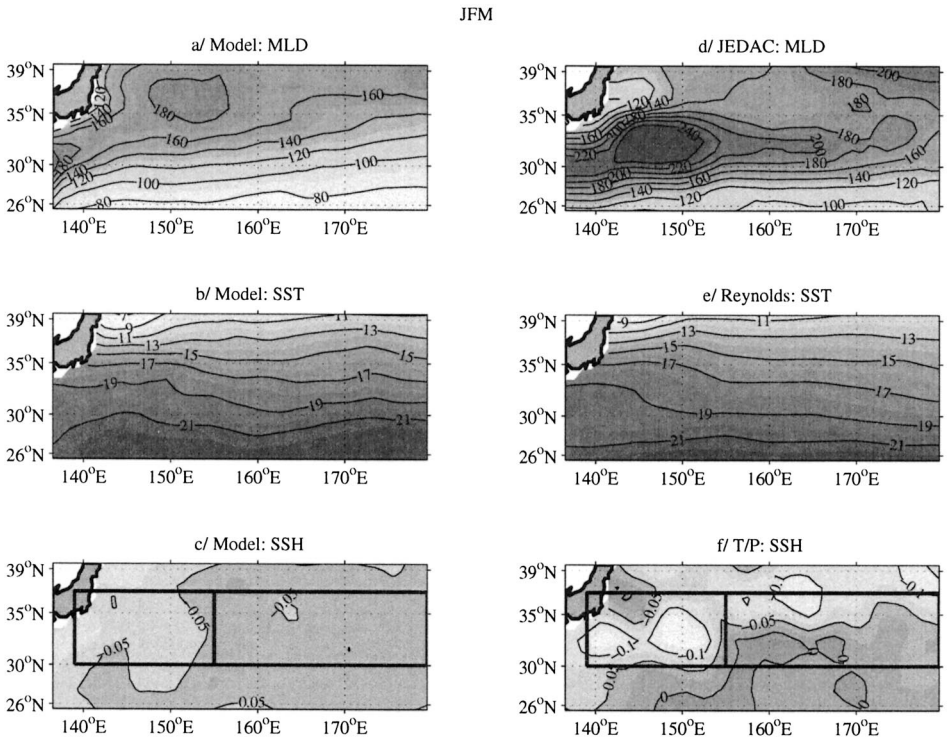

FIG. 7. Winter average (JFM) of (a) the mixed layer depth (m), (b) the SST (°C), (c) and the SSH anomaly (m) derived from the model. (d) MLD is derived from JEDAC dataset, (e) SST is from Reynolds, and (f) SSH is from TOPEX/Poseidon observations. ''Upstream'' and ''downstream'' boxes used for areal averages are indicated for bottom subplots.

generally shallower, the model MLD has a spatial distribution consistent with observations, reaching deeper (180 m) in the path of the Kuroshio in March (Fig. 7; top). Notable differences are found in the Oyashio region possibly as a result of the neglect of salinity effects in the TKE budget. The model wintertime SST shows good agreement with the data (Fig. 7; middle) although it is warmer in the southernmost portion of the domain. The heat content is globally consistent with the SSH from T/P, although spatial variations are not as abrupt in the model (Fig. 7; bottom). Figure 8 depicts the seasonal variations of ΔT, the temperature jump across the base of the ML, averaged over the domain. Although close to 1°C for the annual mean, it undergoes an ample annual cycle, with smallest values ($\Delta T = 0.2$°C) for late winter–early spring, when the ML is deepest.

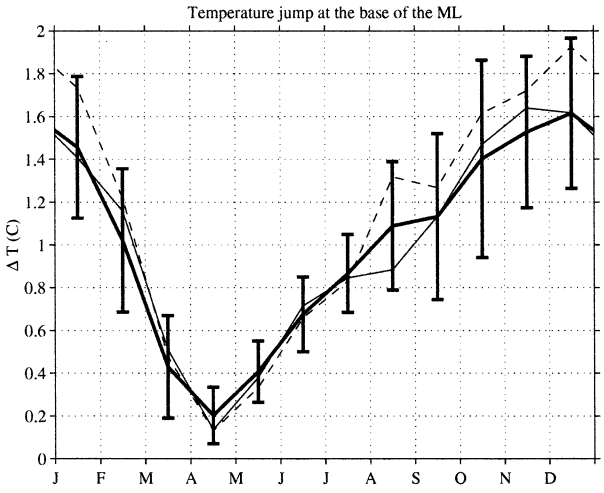

FIG. 8. Seasonal variations of the temperature jump across the base of the mixed layer (°C). Spatial averages are shown for the whole domain (thick), the upstream region (thin line), and the downstream region (thin dashed). The standard deviation throughout the whole domain is indicated.

2) INTERANNUAL VARIATIONS

Qiu (2000) showed substantial interannual variations both in the SSH and in the winter time SST field. For direct comparison with his analyses, we focus on areal averages of the ML depth and temperature, as well as on the SSH over an ''upstream'' (30°–37°N, 139°–155°E) and a ''downstream'' (30°–37°N, 155°E–180°) region, displayed in Fig. 7. Interannual variations for the SST (obtained after subtraction of the monthly averages) are shown in Fig. 9. Interannual variations from observations in the upstream and downstream regions are well correlated in time (0.94 at a lag of 10–20 days; upstream region leading), and both regions exhibit a similar long-term trend of ~0.2°C yr^{-1}. The model SST

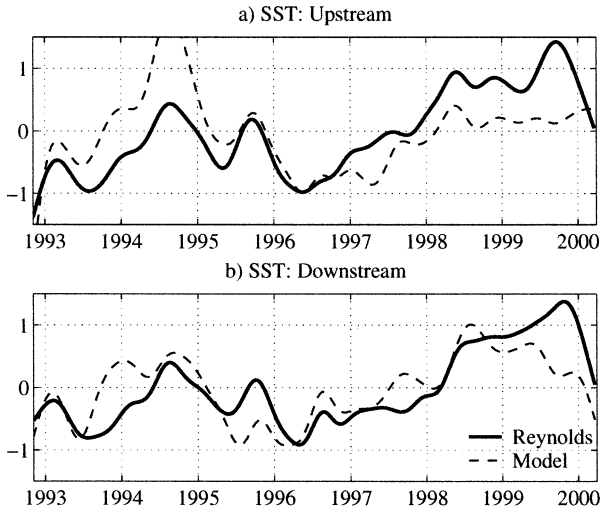

FIG. 9. Domain average of the ML temperature. Nonseasonal SST from Reynolds data (thick) and from the model forced with fluxes from the TOGA COARE bulk algorithm (thin dashed) averaged over (a) the ''upstream'' and (b) ''downstream'' regions displayed in Fig. 7. Series are low-pass filtered with a cutoff period at 200 days for clarity.

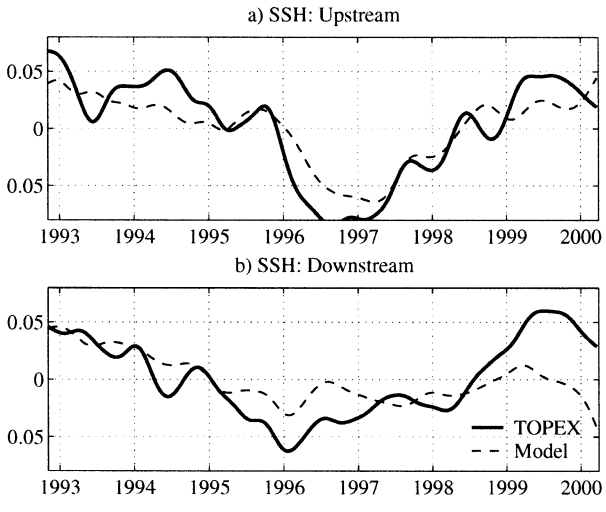

FIG. 10. Domain average of the SSH anomaly. Same as Fig. 9 except for SSH anomaly from the model (dashed) and from TOPEX/Poseidon (thick).

anomaly compares best with observations in the downstream region, but it is noteworthy that the general warming trend is apparent in both regions. The largest discrepancy between model and observations occurs in summer 1994 in the upstream region, with the model presenting an anomaly that is too warm.

Interannual variations of the SSH are shown in Fig. 10. As noted by Qiu (2000), the SSH anomaly from T/P decreases from 1992 to 1996, and increases afterward. More recent data (up to March 2000) are included here, which suggest a break in the increase or the beginning of a decrease after summer 1999. Model-derived SSH anomalies (from the upper 400-m temperature field) reproduce well this picture in the upstream Kuroshio region, while for the downstream region, the comparison breaks down after 1999. It is difficult to assess whether subsurface advection or surface heat flux is at fault here.

4. Heat budget

The model shows reasonable agreement with the observations, making it possible to analyze the different contributions to the heat budget. We first examine the balance of terms responsible for heat content changes in the upper 400 m of the ocean, both on seasonal and interannual timescales, before considering the budget of the SST tendency.

a. Heat budget of the water column

The heat storage rate in the water column is examined at each grid point down to a depth of 400 m only because boundary conditions do not carry interannual changes below that depth. Heat content changes are determined by combining (7) in the ML (after including horizontal processes) and (1) below the ML and integrating vertically. Assuming that no radiative heating escapes the column at 400 m, and remembering that vertical velocity is taken constant with z, one obtains

$$\rho c_p \frac{\partial}{\partial t} \int T\, dz = \rho c_p \int [\kappa_h \nabla^2 T - (\mathbf{u}_g + \mathbf{u}_{\mathrm{Ek}}) \cdot \boldsymbol{\nabla} T]\, dz - \rho c_p w (T_m - T_{400}) + Q_{\mathrm{net}}, \qquad (8)$$

where we have neglected vertical diffusion at 400 m, $\rho c_p \kappa_h \partial T/\partial z$, which for a typical shear of 10^{-2} °C m^{-1} is less than 1 W m^{-2}. In the following analyses, we distinguish the contribution of horizontal advection and diffusion [the first term on the right-hand side of (8)], denoted lateral fluxes for short, vertical Ekman pumping (the second term), and the contribution from surface fluxes Q_{net}.

1) SEASONAL VARIATIONS

Monthly averages have been computed for each term of the heat budget, and these are subsequently zonally averaged over the domain (Fig. 11). The seasonal time rate of change in heat content presents a larger annual cycle to the north of the Kuroshio relative to the south (Fig. 11a). Although surface fluxes partly account for this meridional gradient (Fig. 11c), the contribution from advection–diffusion is substantial (Fig. 11b). North of the Kuroshio, advection acts together with surface fluxes with comparable magnitude (~150 W m^{-2} at 38°N). Figure 12 details spatially the time rate of change in heat content caused by lateral fluxes for wintertime (December–March), contrasted to the rest of the year. In winter, the configuration of warming and cooling is more complex than the zonal average of Fig. 11b may suggest. Indeed, warming by advection is only ob-

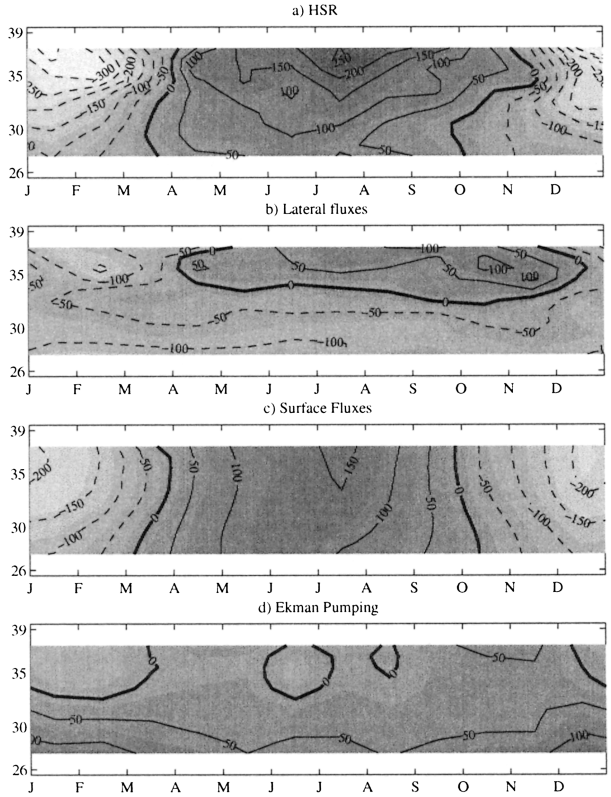

FIG. 11. Zonal average of the monthly mean of the terms of the vertically integrated heat equation: (a) heat storage rate, and contributions from (b) lateral (advection and diffusion) heat flux, (c) surface heat flux, and (d) vertical Ekman pumping (units are W m^{-2}).

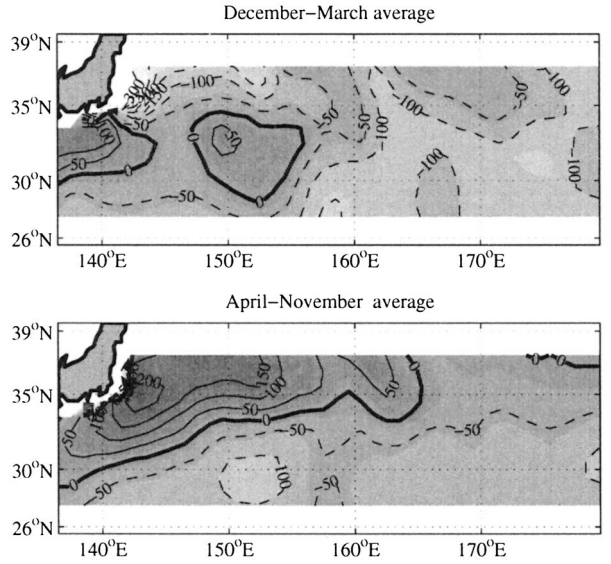

FIG. 12. Lateral fluxes of heat (geostrophic and Ekman advection + diffusion) averaged for (top) winter months and (bottom) for the rest of the year (Apr–Nov; units are W m^{-2}).

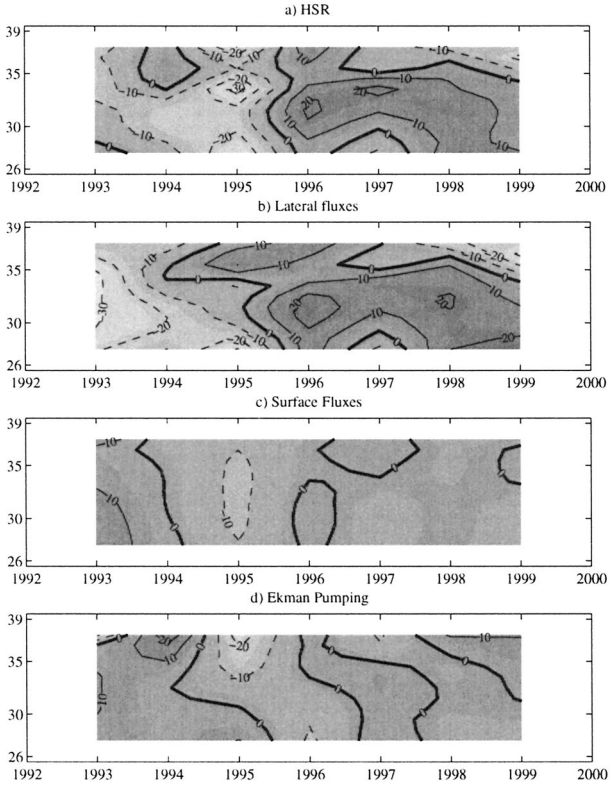

FIG. 13. Same as Fig. 11 but for nonseasonal variations, where annual averages for years 1993–99 are shown.

served in the southwestern corner of the domain, that is, in the upstream Kuroshio and its recirculation gyre, west of 155°E, while cooling prevails elsewhere due to intense Ekman advection, as well as from geostrophic advection of cold Oyashio waters north of 34°N. Part of this cooling north of 35°N is caused by upwelling (~ -30 W m^{-2} on average; not shown), while downwelling occurs south of the Kuroshio, causing a typical warming of the column of ~ 70 W m^{-2} in winter (not shown). During the rest of the year (Fig. 12b), the configuration is more zonal with warming occurring everywhere north—as well as on the path—of the Kuroshio. Cooling is observed south of the Kuroshio as a result of Ekman advection, but also due to southward geostrophic advection within the recirculation gyre that carries colder water to the south.

2) INTERANNUAL CHANGES

Nonseasonal variations are obtained after removing the seasonal cycle and averaging over each year. Interannual changes in heat storage rate are different to the north and to the south of the Kuroshio, but in both regions, these are dominated by changes in advection. This appears clearly after zonally averaging the terms of the heat budget (Fig. 13). South of 35°N, the heat content has decreased until 1995 (negative time rate of

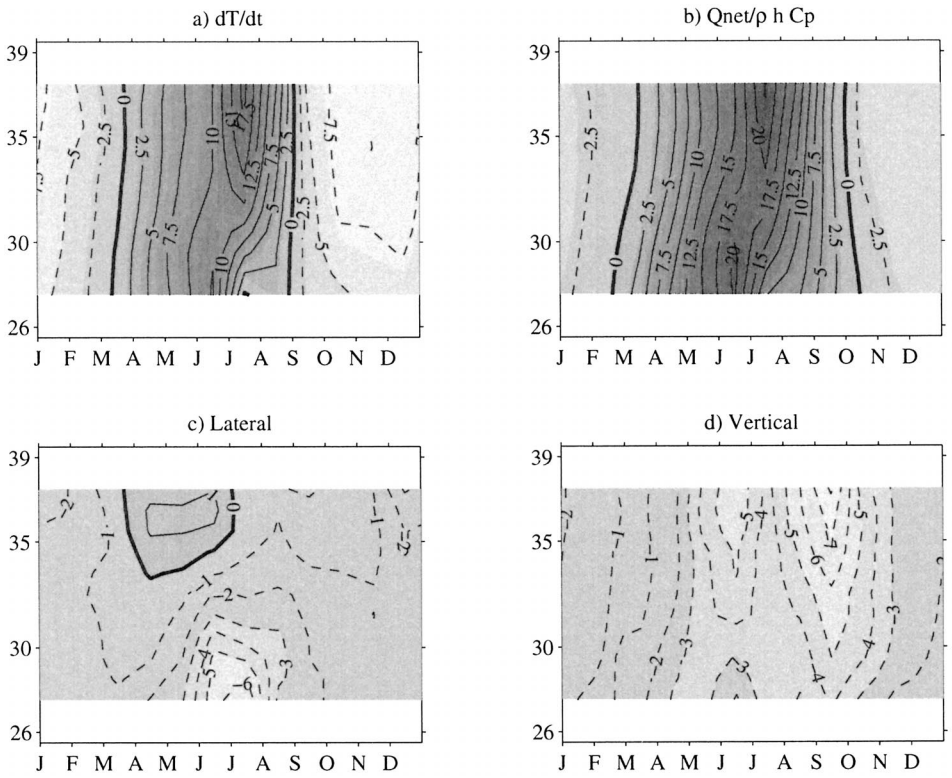

FIG. 14. Zonal average of the monthly mean of the different terms of the temperature tendency equation: (a) temperature tendency, (b) surface fluxes, (c) advection–diffusion (including Ekman advection), and (d) entrainment. Note that the contour interval is different for the last two subplots (units are 10^{-7} °C s^{-1}).

change in Fig. 13a), and increased after 1996. This corresponds to the transition from an elongated state of the Kuroshio to a contracted state in 1995 and back to an elongated state described by Qiu (2000). North of 35°N, the picture is more complex, with the heat content generally decreasing except for 1994 and 1996 with two abrupt positive anomalies. Figure 13a looks very much like Fig. 13b suggesting that lateral fluxes of heat (mainly changes in advection) are primarily responsible for the heat content changes, both cooling up to 1995 and warming afterward. The influence of surface fluxes appears less important on the nonseasonal time rate of change in heat content (Fig. 13c). There is however a notable negative anomaly in 1995 of -10 W m^{-2} contributing, together with advection, to the cooling of the column. Ekman pumping has also a moderate influence, except north of 35°N.

b. Mixed layer temperature tendency budget

We now focus on the heat budget of the ML, examining the different terms of the temperature tendency equation (7). The latter, after including the contribution from advection and diffusion, reads

$$\frac{\partial T_m}{\partial t} = \kappa_h \nabla^2 T_m - (\mathbf{u}_g + \mathbf{u}_{\mathrm{Ek}}) \cdot \boldsymbol{\nabla} T_m + \frac{Q_{\mathrm{net}} - q(-h)}{\rho c_p h} - \frac{\Delta T w_e}{h} \mathcal{H}(w_e), \tag{9}$$

where $\mathcal{H}(w_e)$ is the Heaviside step function. We will distinguish the temperature tendency term [left-hand side of (9)], the advection–diffusion term (first three terms of the right-hand side, including both geostrophic and Ekman advection), the surface flux term, and the entrainment term (the latter also includes the contribution from convective overturning, which turns out to be negligibly small at these latitudes). As in the previous section, we first focus on seasonal variations, before discussing interannual changes.

1) SEASONAL VARIATIONS

Consistent with the results of Qiu and Kelly (1993), Fig. 14 shows that the warming contribution of the surface thermal forcing dominates the temperature tendency from April to July, the period during which the deep winter ML erodes on average. Entrainment contributes to cool the ML layer almost all of the year. Indeed, since the erosion of the ML is not a monotonic process, colder

water from below is constantly being incorporated to the ML by entrainment, due to day-to-day changes of the ML depth (a sudden deepening of the ML followed by a retreat to its original depth will result in a heat loss for the ML as entrainment is a nonsymmetric process). Cooling by entrainment is nevertheless strongest between May and October, especially to the north of the Kuroshio and is the second largest contribution (Fig. 14d). It culminates in September, where the shallow ML (thus with little thermal inertia) deepens rapidly. The cumulated contribution of geostrophic advection, Ekman advection, and diffusion is the smallest term of the zonally averaged temperature tendency budget. Its most salient features are a cooling south of the Kuroshio, and a warming in spring north of 35°N (the latitude where warm eddies are shed). As noted by Qiu and Kelly (1993), who provide the break down of these terms, these contribute unevenly in the various parts of the domain, except for the Ekman advection (not shown) whose contribution is globally negative for most of the year, due to a downgradient Ekman transport (to the south). Lateral processes significantly warm the upstream Kuroshio region (west of 155°E), mainly from geostrophic advection and eddy shedding, whereas they cool the downstream region, not only because of Ekman advection, but also due to geostrophic advection in the southward recirculation gyre that carries colder waters from the north.

The annual mean of the different contributions to the heat budget are shown in Fig. 15. Surface heat fluxes have a warming contribution (Fig. 15b). This effect is initially surprising since the ocean loses heat over most of the domain, but, as was noted by Qiu and Kelly (1993), changes in MLD act as a powerful filter giving more weight to summer warming over shallow ML, than to winter cooling over deep ML. Surface fluxes are primarily balanced by entrainment and to a lesser extent by lateral fluxes, except to the northwest of the domain where advection has a warming contribution (via eddy shedding). If we average over the domain considered by Qiu and Kelly (1993) (30°–40°N, 141°–175°E) we find 4.6×10^{-7}, -3.4×10^{-7}, and -1.1×10^{-7} °C s^{-1} for surface fluxes, entrainment, and horizontal processes, respectively, whereas their Table 1 yields 3.2×10^{-7}, -1.1×10^{-7}, and -2.1×10^{-7} °C s^{-1}. Although these numbers are consistent (e.g., lateral fluxes globally cool the region in both models in the annual mean), we find on the contrary that entrainment is the main term balancing surface fluxes. Many parameters differ between the two models (for instance the diffusion coefficient is ~2.5 times larger in their case) and the forcing fields are different, but it is likely that larger values found for entrainment here are attributable to the fact that we do not assume a constant jump of 1°C across the base of the ML.

2) INTERANNUAL CHANGES

We now consider annual averages of the different nonseasonal terms of the temperature tendency equation

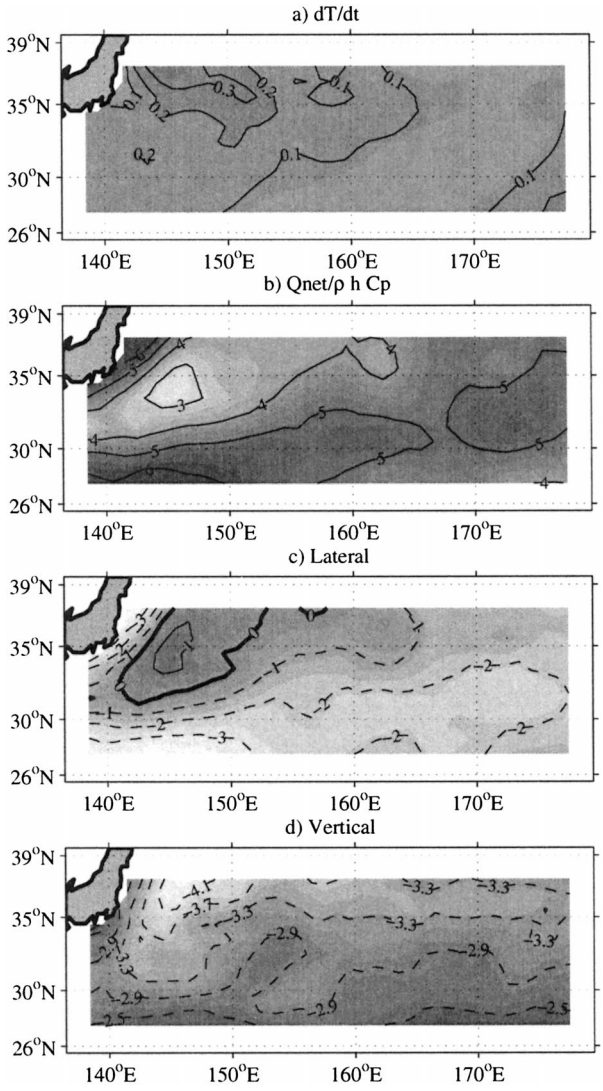

FIG. 15. Same as Fig. 14 but for annual mean of the different terms contributing to the temperature tendency equation in the ML (units are 10^{-7} °C s^{-1}).

(Fig. 16). Although the temperature tendency appears to be mostly negative in Fig. 16a, it is not inconsistent with the fact that temperature increases on the long term, since the seasonal $\partial T/\partial t$ does not average to zero (see Fig. 15a). A striking aspect of Fig. 16 is that none of the three processes considered (surface fluxes, entrainment and advection) have negligible contributions to the nonseasonal temperature tendency. This differs from the interannual budget of heat content in the upper 400 m, for which advection dominates. The nonseasonal $\partial T/\partial t$ is positive in 1993 and decreases to negative values in 1995 before abruptly peaking in 1996, and then slowly decaying again until 1999. These time variations are mostly matched by changes in surface fluxes (Fig. 16b) and lateral processes (Fig. 16c), while the contribution from nonseasonal entrainment reaches its largest vari-

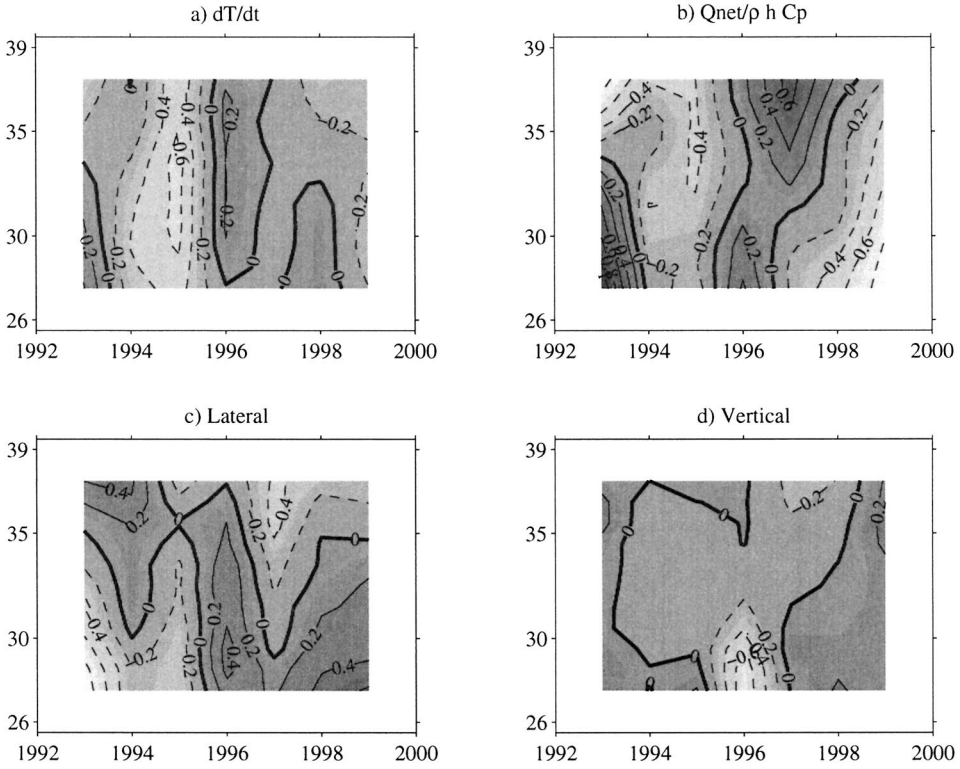

FIG. 16. Same as Fig. 14 but for zonal average of the different terms of the temperature tendency equation on interrannual timescales: temperature tendency, surface fluxes, advection–diffusion, and entrainment (units are 10^{-7} °C s^{-1}).

ations only south of 32°N. While both surface fluxes and advection are responsible for the decrease up to 1995, the sharp rise in 1996 is mainly attributable to advection.

It is interesting to note that nonseasonal entrainment appears to be accompanying changes caused by geostrophic advection (Fig. 16d). When the Kuroshio is in an elongated state (1993 and 1998) entrainment contributes in general positively to the temperature tendency, that is less heat is taken out of the ML. Whereas in 1995–96, when the Kuroshio is in a contracted state, the efficiency of entrainment in cooling the ML is increased. This suggests that the subsurface thermal content (driven primarily by horizontal advection on interannual timescales) has a direct impact on nonseasonal entrainment. To further assess this mechanism we have run the model again in a ''climatological'' mode; that is, at each time step, the thermal field from the *WOA98* is inserted below the ML. By doing this, we ensure that there are no interannual heat content changes except for those caused by temperature changes within the ML. All other parameters and forcings from the reference model run are kept unchanged. Figure 17a shows that the nonseasonal SST is larger in the reference run compared with the climatological run, bearing larger interannual variations. Although advection (through lateral induction) explains part of these differences in the SST, Fig. 17b shows that, in addition, less heat is taken out of the ML by entrainment in the reference experiment compared with the climatological run. In the latter case, the heat content is smaller below the ML (with no interrannual variations) as indicated by the temperature at 125 m, within the seasonal thermocline (Fig. 17a).

Qiu (2000) focus on the wintertime temperature tendency budget (as opposed to anomalies from the annual mean here) and finds only a small contribution from entrainment. Accordingly, the nonseasonal $\partial T/\partial t$ budget restricted to JFM shows that $\partial T/\partial t$ is matched by surface and lateral fluxes, whereas entrainment plays a smaller role (not shown), a result that is not totally surprising considering that vertical entrainment of heat is largest during the fall (Fig. 14d), not winter. Nonetheless, wintertime SST (not its tendency) is affected by anomalies in entrainment occuring before winter (e.g., Alexander and Deser 1995).

5. Summary and conclusions

The present study was motivated by understanding the origins of the interannual variability observed both in SST and SSH in the KE region by Qiu (2000). It has been recognized that interannual changes in SST in this region are part of the large-scale horseshoelike pattern associated with the PDO, that varies on decadal time-

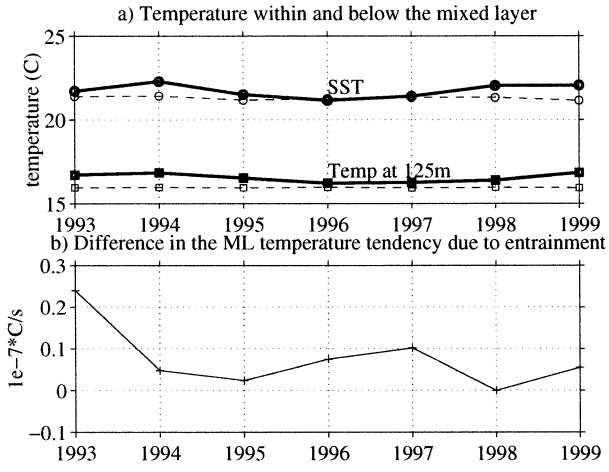

FIG. 17. Influence of the subsurface heat content on the nonseasonal SST through the entrainment process: (a) temperature within the ML (circles) and at a depth of 125 m (squares) averaged over the domain, for the reference experiment (bold line) and for the climatological model run (dashed line). ML temperature are annual averages whereas subsurface temperature are summer averages (May–Aug), to ensure that the depth of 125 m is within the seasonal thermocline. (b) Difference in entrainment-related ML temperature tendency for the reference experiment relative to the climatological run. Domain average of the annual mean is shown. Positive values indicate that less heat is extracted from the ML by entrainment in the reference run compared with the climatological run. In the latter case, the heat content is smaller as indicated by the temperature at 125 m shown in (a).

scales. There is a suggestion that the PDO might have switched in 1998 from a ''warm'' phase (characterized in the KE region by a cold core of SST anomalies) to a ''cold'' phase (Fig. 1). In this context, the analysis of the heat budget in the KE region between 1993 and 1999 is particularly timely and relevant, as it provides the opportunity to examine changes in the processes (be they oceanic or atmospheric) affecting the SST and ocean heat content, that have accompanied these variations in the PDO index.

The analysis of the heat budget in the KE region is complicated by the fact that horizontal advection cannot be ignored (Qiu and Kelly 1993). This has prompted us to develop a 3D advection–diffusion finite-element model of the temperature field in the upper ocean (0–800 m), coupled, as per Adamec et al. (1981), to a bulk mixed layer model based on the parameterization of Gaspar (1988). Following Qiu and Kelly (1993), geostrophic advection is determined externally using TOPEX/Poseidon altimeter data, whereas Ekman advection and vertical Ekman pumping are derived from the wind field. The temperature field is imposed at the boundaries, and is taken from XBT data compiled by the JEDAC down to 400 m, while climatology is used below. The model is forced with the daily wind stress, and radiative heat fluxes from the NCEP reanalysis project. The use of turbulent (latent and sensible) heat fluxes from NCEP yields an interannual cooling trend in the SST computed with the model, suggesting that this product overestimates heat losses to the atmosphere in winter time, when strong wind conditions prevail, consistent with an analysis of Zeng et al. (1998). To correct for this pitfall, we have derived alternate turbulent heat fluxes products based on two different paramerizations of the atmospheric boundary layer: Kondo–Smith on the one hand, and COARE 2.5b on the other hand, the latter leading to a better agreement between model SST and observations. However, in the present setting of the model, relatively crude assumptions made as for subsurface horizontal advection do not permit us to be more definite in validating one heat flux parameterization against the other.

Despite these restrictions, the present model, which includes key processes for the evolution of SST (advection, subsurface layers that preserve the year-to-year memory of the temperature changes) yields reasonable agreement both for seasonal and interannual variations of the SST compared with observations. The variations of the heat content of the upper 400 m of the model is also well correlated with T/P data, although with a smaller seasonal cycle. In the data, SST and SSH vary consistently on interannual timescales, with 1997 being a ''hinge'' year. While SST presents a general warming trend over the domain between 1992 and 2000, the warming increases after 1997. The SSH, a proxy for the heat content, exhibits a decreasing trend up to 1996–97 before increasing abruptly up to 1999. Both of these features are relatively well reproduced by the model (e.g., Figs. 9, 10).

The model has been used to examine the heat budget in the upper 400 m of the ocean, as well as in the mixed layer (SST tendency budget). On seasonal timescales, both surface heat fluxes and horizontal advection contribute substantially to heat content changes. As for the ML temperature tendency, the seasonal budget is consistent with the analysis by Qiu and Kelly (1993): we find that heat fluxes are the major contribution, with seasonal variations ~4 times larger than entrainment or advection. However, in the annual mean, we find that, generally, entrainment at the base of the ML is the main mechanism that opposes heat fluxes, contrary to horizontal processes in their study. Nonetheless, horizontal processes are found to be dominant in the annual mean heat budget of the upper 400 m of the ocean, especially in the upstream Kuroshio region. This suggests that lateral fluxes of heat in the subsurface ultimately affect the ML temperature after waters advected below the ML have been entrained, a process that appears more important in the annual mean than horizontal advection within the ML.

On interannual timescales, further analyses of the 0–400-m heat budget show that the nonseasonal heat storage rate is dominated by changes in horizontal fluxes (advection/diffusion) of heat. These lateral fluxes induce changes in heat content, the signature of which in terms of SSH accounts well for the transitions between an elongated and a contracted state of the KE and its re-

circulation gyre observed in altimeter data by Qiu (2000). The nonseasonal mixed layer temperature tendency budget is more complex. We find that none of the processes considered (nonseasonal air–sea heat fluxes, horizontal advection–diffusion and vertical entrainment) have a negligible impact on the nonseasonal SST field. Anomalous surface heat fluxes are considered to be the dominant cause for nonseasonal SST changes in the midlatitudes (Cayan 1992). Figure 16b shows that their contribution is also important in the KE region. However, oceanic processes also contribute substantially to the generation of SST anomalies. In particular, the transition between an elongated and a contracted state of the Kuroshio caused by geostrophic advection has a clear signature on the SST, in agreement with the analysis of Qiu (2000). There is an indication that this process is accompanied by consistent changes in the nonseasonal entrainment: in the elongated state, when warmer waters are present below the ML, entrainment appears less efficient in exporting heat out of the ML (resulting in positive entrainment anomalies in the nonseasonal heat budget), while the opposite holds true for the contracted state. Consistent with the results of Xie et al. (2000), this study suggests that subsurface variability impacts SST in the Kuroshio region. Away from western boundaries, Alexander and Deser (1995) showed that wintertime SST is affected by anomalous entrainment due to reemerging temperature anomalies from the previous winter. While this is intrisically a local process, it does not hold where advection is important. Rather, this study suggests a double effect of advection on the nonseasonal SST. First, it directly affects SST by lateral fluxes of heat within the ML. In addition, as advection dominates the nonseasonal heat storage rate within the water column (Fig. 13), it modifies the thermal structure below the ML as well, further impacting SST changes by anomalous entrainment. This is suggested by Fig. 16 which shows that advection and entrainment team up to increase the SST after 1997, opposing the surface heat flux contribution.

Although the analyses presented here are not appropriate to discuss the merits of the different PDO theories, we note that the influence of ocean dynamics (both advection and entrainment) in the nonseasonal SST field in the Kuroshio region is compatible with theories that involve an active role from ocean dynamics, be it within a coupled ocean–atmosphere mode or a forced mode scenario. A recent study with a coupled model by Schneider et al. (2002) suggests a coupled mode of decadal variability with SST anomalies in the KE region originating below the mixed layer by pertubation of the streamfunction caused by Rossby waves. In this mode, SST anomalies are damped by turbulent air–sea fluxes, thus forcing the midlatitude atmosphere. We note that Fig. 16 is compatible with their finding after 1997, suggesting that an excess of heat from the ocean (both from advection and entrainment) is vented to the atmosphere (negative surface fluxes). However, the question of the origin of the observed bimodality (elongated/contracted) of the KE system, whether it comes from wind driven changes, intrinsic dynamics of the western boundary current (Qiu and Miao 2000), or multiple equilibria theories (Schmeits and Dijkstra 2001; Cessi and Ierley 1995) (with a potential influence of wind forcing as a trigger for mode switching), cannot be addressed here. Longer series of altimeter data would certainly be needed to investigate this question.

Acknowledgments. The authors would like to thank Bo Qiu for providing the mean SSH. Enlightening discussions with Ralph Foster (UW/APL) and Jerome Patoux (Department of Atmospheric Sciences/UW) about similarity theories of the planetary boundary layer, as well as their help with the use of the UW planetary boundary layer model, are gratefully acknowledged. Fluxes computations involving the TOGA COARE algorithm have been performed with the AirSea toolbox for MATLAB developed by B. Beardsley and R. Pawlowicz. Helpful discussions with Chris Fairall and Xubin Zeng have also been very much appreciated. Valuable comments from the reviewers were very helpful and appreciated. The PDO index was obtained online from the University of Washington's Joint Institute for the Study of the Atmosphere and Oceans Web site: http://jisao.washington.edu/pdo. Funding for this research was provided by NASA through Grant NAG5-8296 (FV, KAK) and by NSF through Grant OCE-9818920 (LT, KAK).

APPENDIX A

Correction to the Mean SSH

In this appendix we propose a correction to the mean SSH field based on minimizing the residual of the long-term (1992–2000) averaged heat budget, as per Kelly and Qiu (1995a), but using instead a variational approach inspired by Vigan et al. (2000).

We examine the residual R of the time-averaged heat equation, defined by

$$R = \left\langle \partial_t T + \frac{g}{f}\mathcal{J}(\eta, T) + \frac{1}{h}\mathbf{U}_{\mathrm{Ek}} \cdot \boldsymbol{\nabla} T + \frac{\Delta T w_e}{h} - \frac{Q - q_d}{\rho c_p h} - \kappa_T \nabla^2 T \right\rangle, \quad \text{(A1)}$$

where $\mathcal{J}$ is the Jacobian with respect to x and y, and η is the SSH from T/P. Model forcing from NCEP and temperature observations from *WOA98* were used to estimate the different terms needed in (A1) to compute the residual R.

The logic followed here is to attribute most of the errors leading to a nonzero residual to the mean advection term (although certainly not totally, the later may contribute substantially to nonzero residual). Thus, we search for a correction $\epsilon(x, y)$ to the mean SSH field

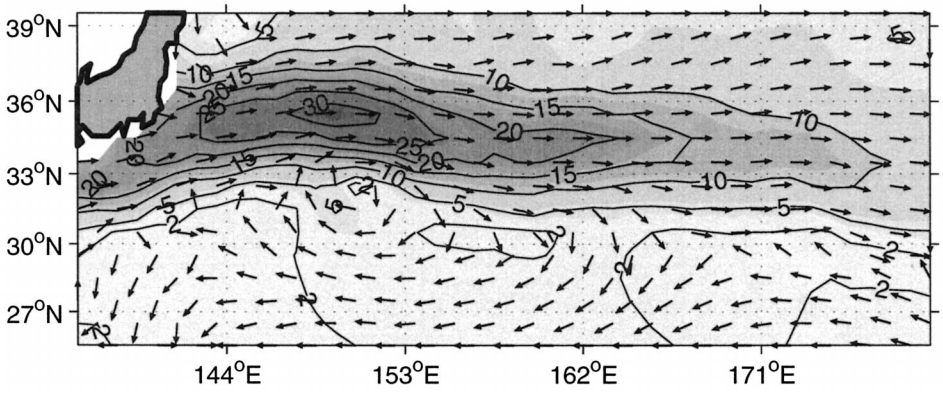

FIG. A1. Mean geostrophic velocity, after correction. Arrows have unit length and indicate direction only whereas the modulus is contoured (cm s^{-1}).

such that it minimizes over the domain Ω the following functional:

$$\mathcal{F}(\epsilon) = \int_\Omega [\mathcal{J}(\epsilon, \langle T\rangle) + R]^2 \, d\Omega. \quad \text{(A2)}$$

Denoting υ any variation $\delta\epsilon$ (which satisfies $\delta\epsilon = 0$ on $\partial\Omega$), $\mathcal{F}$ is stationary if

$$\delta\mathcal{F} = 0 = \int_\Omega (\langle T\rangle_y \epsilon_x - \langle T\rangle_x \epsilon_y + R) \times (\langle T\rangle_y \upsilon_x - \langle T\rangle_x \upsilon_y) \, d\Omega. \quad \text{(A3)}$$

We search for an approximation of ϵ decomposed on the basis of ''hat'' functions defined on the triangular mesh, and we solve (A3), with variations υ also taken as ''hat'' functions. The problem is underdetermined without additional constraint or boundary conditions, since the residual of the heat equation provides only information of the local SSH slope, not on the SSH itself. A natural additional constraint is to impose the correction to have minimum energy (minimum quadratic norm), by considering instead of $\mathcal{F}$, the functional $\mathcal{F}'$ of the form

$$\mathcal{F}' = \mathcal{F} + \alpha^2 \int_\Omega \epsilon^2 \, d\Omega. \quad \text{(A4)}$$

The parameter α, which determines the relative weight of the physical constraint to be enforced (a balanced heat budget on the long term) and of the minimum energy constraint, has been set to $0.2|K|/|M|$, where $|K|$ and $|M|$ are the norm of the matrices associated with the discretized version of $\mathcal{F}(\epsilon)$, and of the minimum energy constraint respectively, as a trade-off between the misfit to Eq. (A2) (25% of the norm of the residual R) and the variance of the correction (3–4 cm rms).

The ''corrected'' mean geostrophic velocity field is shown in Fig. A1. Compared with the original velocity field of Fig. 2b, the correction has brought interesting modifications. First, the two quasi-stationnary meanders of the Kuroshio have been smeared out. While we do not claim that the field thus obtained is more representative of the mean circulation in the Kuroshio region, it is certainly more consistent, in terms of spatial resolution, with the SST observations we used. One also notes that the wiggles in the velocity field north of the Kuroshio extension have disappeared. In this case, the correction is actually removing an artefact of the mapping of altimeter data. Interestingly, the velocity field has also been significantly modified in the Oyashio region, yielding southward velocities on the order of 5 cm s^{-1}, instead of eastward velocities before.

APPENDIX B

Coupling of the Mixed Layer to the Advection–Diffusion Model

This appendix describes the method of embedding the ML model in the tridimensional AD model, which is adapted from Adamec et al. (1981) for the finite element grid, with also some changes as to how convective adjustment is handled. As the nodes of the mesh are aligned in the vertical (the triangular mesh on each level mirrors adjacent levels), elements can be considered as line segments as far as coupling between the ML and layers below is concerned. Assuming that we initially know the 3D temperature field T below the ML, as well as h, T_m, and T_b (temperature within and at the base of the ML), the scheme is as follows:

1) Insertion of the discontinuous temperature profile into the 3D grid: Assuming that h lies within element l_k (that is between node k and $k + 1$; Fig. B1a), the temperature T_{k+1} at the node immediately below the mixed layer interface is modified before the AD step in order to suppress the discontinuity, in such a way that the heat content is the same in the two piecewise linear profiles; that is,

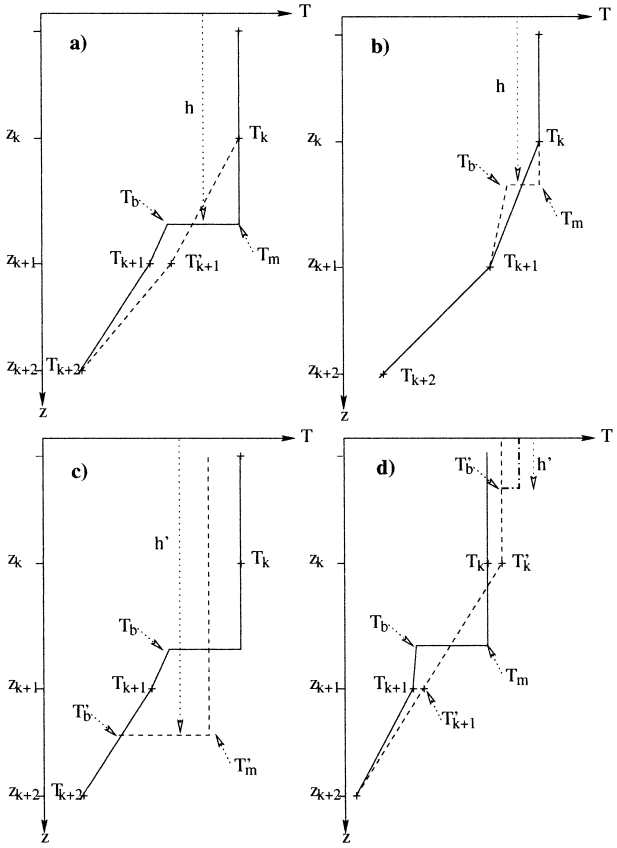

FIG. B1. Coupling of the ML and AD model. (a) Inclusion of the mixed layer into the 3D grid. The temperature T_{k+1} of the grid point immediately below the mixed layer interface is modified (dashed line) before the advection diffusion step so that the heat content is the same in the two piecewise linear profiles. (b) Restoration of the discontinuous vertical profile of temperature (dashed line). (c) Entrainment phase: the new (dashed) and old (solid) temperature profile have same heat content. (d) Detrainment phase: the new profile (dashed) has same heat content and potential energy as the old profile (solid). The new ML of depth h' only appears in the temperature profile after heat is exchanged with the atmosphere (dash–dot line).

$$T'_{k+1} = \frac{z_{k+2} - h}{z_{k+2} - z_k} T_{k+1} + \frac{h - z_k - z_{k+1}}{z_{k+2} - z_k} T_m + \frac{z_{k+1} - h}{z_{k+2} - z_k} T_b. \tag{B1}$$

2) Advection–diffusion of T according to (1).
3) Advection–diffusion of h.
4) Restoration of the discontinuous temperature profile: After the AD of the temperature field, and prior to considering buoyancy changes due to vertical entrainment, it is necessary to reconstruct an updated temperature jump at the base of the ML, which depth h has also changed by AD. Assuming that h falls between nodes k and $k + 1$ (Fig. B1b), T_m is set to T_{k-1} and T_b is set so as to preserve heat in the column:

$$T_b = T_k + \frac{h - z_k}{z_{k+1} - h}(T_{k+1} - T_m). \tag{B2}$$

After T_b is obtained, the temperature T_m is homogenized by mixing within the ML. Instabilities that may occur below the ML are removed by convective adjustment, following the algorithm of Rahmstorf (1993). The next step is to ensure that $T_m \geq T_b$. If not, the ML convectively deepens down to that depth where stability is restored, and the ML temperature is modified accordingly.

5) Changes of h due to turbulent processes, according to either (4) or (6) depending on whether the ML is entraining (detraining): Note that the temperature jump across the base of the ML, $\Delta T = T_m - T_b$, is known everywhere.
6) Changes of temperature due to entrainment/detrainment.

6a) Entrainment: At those grid points where the ML deepens to a new depth h', it mixes waters with temperature T_b at the base of the ML, but increasingly colder below. The new temperature in the ML is calculated so that the heat incorporated in the deepening phase is homogeneously distributed through the new depth h' (Fig. B1c). The new T_b is simply obtained by interpolation of the linear profile at the base of the new mixed layer.

6b) Detrainment: When the mixed layer shoals, the temperature profile is theoretically unchanged. However, following Adamec et al. (1981), provision must be made for the fact that part of the information about the stratification at the base of the ML depth (prioir detrainment) will be lost on the coarse vertical grid at the next time step. Consequently, the temperature at the node immediately below the old ML depth (T_{k+1}), as well as at those levels encompassed in the ML (T_m), is modified so that heat and potential energy of the water column are unchanged (Fig. B1d). For one element, potential energy and heat content are given by

$$E_p(l_k) = -T_k \int_{z_k}^{z_{k+1}} z\Phi_k(z)\, dz - T_{k+1} \int_{z_k}^{z_{k+1}} z\Phi_{k+1}(z)\, dz, \tag{B3}$$

$$E_i(l_k) = T_k \int_{z_k}^{z_{k+1}} \Phi_k(z)\, dz + T_{k+1} \int_{z_k}^{z_{k+1}} \Phi_{k+1}(z)\, dz, \tag{B4}$$

where $\Phi_j(z)$ are the two basis function defined over the element l_k.[B1] Summing (B3) and (B4) over the water column yields a system of two equations in

[B1] $\Phi_k(z) = (z - z_{k+1})/(z_k - z_{k+1})$ and $\Phi_{k+1}(z) = (z - z_k)/(z_{k+1} - z_k)$.

the two unknowns T'_{k+1} and T'_m (Fig. B1d). Note that the new shallower ML does not actually show up in the temperature profile until heat is exchanged with the atmosphere.

7) Surface fluxes. The temperature of the newly formed mixed layer is finally changed by surface fluxes [according to (7), save for the entrainment term]. Convective deepening may again occur for unstable situations. The 3D temperature field T, h, and T_b are then stored and the whole process is reiterated.

REFERENCES

Adamec, D., R. L. Elsberry, R. W. Garwood, and R. L. Haney, 1981: An embedded mixed-layer ocean circulation model. *Dyn. Atmos. Oceans*, **6,** 69–96.

Alexander, M. A., and C. Deser, 1995: A mechanism for the recurrence of wintertime midlatitude SST anomalies. *J. Phys. Oceanogr.,* **25,** 122–137.

——, J. D. Scott, and C. Deser, 2000: Processes that influence sea surface temperature and ocean mixed layer depth variability in a coupled model. *J. Geophys. Res.,* **105,** 16 823–16 842.

Antonov, J., S. Levitus, T. P. Boyer, M. Conkright, C. O'Brien, and T. D. Stephens, 1998: *Temperature of the Atlantic Ocean.* Vol. 1, *World Ocean Atlas 1998,* NOAA Atlas NESDIS 27, 166 pp.

Auad, G., A. J. Miller, and W. B. White, 1998: Simulation of heat storages and associated heat budgets in the Pacific Ocean, Part 1: El Niño–Southern Oscillation timescale. *J. Geophys. Res.,* **103,** 27 603–27 620.

Battisti, D. S., U. S. Bhat, and M. A. Alexander, 1995: A modeling study of the interannual variability in the wintertime North Atlantic Ocean. *J. Climate,* **8,** 3067–3083.

Brown, R. A., and W. T. Liu, 1982: An operational large-scale marine planetary boundary layer model. *J. Appl. Meteor.,* **21,** 261–269.

Cayan, D. R., 1992: Latent and sensible heat flux anomalies over the northern oceans: Driving the sea surface temperature. *J. Phys. Oceanogr.,* **22,** 859–881.

Cessi, P., and G. R. Ierley, 1995: Symmetry-breaking multiple equilibria in quasigeostrophic, wind-driven flows. *J. Phys. Oceanogr.,* **25,** 1196–1205.

Chelton, D. B., and M. G. Schlax, 1994: The resolution capability of an irregularly sampled dataset: With application to Geosat altimeter data. *J. Atmos. Oceanic Technol.,* **11,** 534–550.

Deser, C., M. A. Alexander, and M. S. Timlin, 1999: Evidence for a wind-driven intensification of the Kuroshio Current extension from the 1970s to the 1980s. *J. Climate,* **12,** 1697–1706.

Fairall, C. W., E. F. Bradley, D. P. Rogers, J. B. Edson, and G. S. Young, 1996: Bulk parameterization of air–sea fluxes for Tropical Ocean–Global Atmosphere Couple Ocean Atmosphere Response Experiment. *J. Geophys. Res.,* **101,** 3747–3764.

Frankignoul, C., 1985: Sea surface temperature anomalies, planetary waves, and air–sea feedback in the middle latitudes. *Rev. Geophys.,* **23,** 357–390.

——, P. Müller, and E. Zorita, 1997: A simple model for the decadal response of the ocean to stochastic wind forcing. *J. Phys. Oceanogr.,* **27,** 1533–1546.

Gaspar, P., 1988: Modeling the seasonal cycle of the upper ocean. *J. Phys. Oceanogr.,* **18,** 161–180.

Jin, F.-F., 1997: A theory of interdecadal climate variability of the North Pacific ocean–atmosphere system. *J. Climate,* **10,** 1821–1835.

Kalnay, E., and Coauthors, 1996: The NCEP/NCAR 40-Year Reanalysis Project. *Bull. Amer. Meteor. Soc.,* **77,** 437–471.

Kelly, K. A., and S. T. Gille, 1990: Gulf Stream surface transport and statistics at 69°W from Geosat altimeter. *J. Geophys. Res.,* **95,** 3146–3161.

——, and B. Qiu, 1995a: Heat flux estimates for the western North Atlantic. Part I: Assimilation of satellite data into a mixed layer model. *J. Phys. Oceanogr.,* **25,** 2344–2360.

——, and ——, 1995b: Heat flux estimates for the western North Atlantic. Part II: The upper ocean heat balance. *J. Phys. Oceanogr.,* **25,** 2361–2373.

Kondo, J., 1975: Air–sea transfer coefficients in diabatic conditions. *Bound.-Layer Meteor.,* **9,** 91–112.

Latif, M., and T. P. Barnett, 1994: Causes of decadal climate variability over the north Pacific and North America. *Science,* **266,** 634–637.

Mantua, N. J., S. R. Hare, Y. Zhang, J. M. Wallace, and R. C. Francis, 1997: A Pacific decadal climate oscillation with impacts on salmon. *Bull. Amer. Meteor. Soc.,* **78,** 1069–1079.

Miller, A. J., D. R. Cayan, and W. B. White, 1998: A westward-intensified decadal change in the North Pacific thermocline and gyre-scale circulation. *J. Climate,* **11,** 3112–3127.

Niiler, P. P., and E. B. Kraus, 1977: One-dimensional models of the upper ocean. *Modelling and Prediction of the Upper Layers of the Ocean,* E. B. Kraus, Ed., Pergamon Press, 152–172.

Ostrovskii, A. G., and L. I. Piterbarg, 2000: Inversion of upper ocean temperature time series for entrainment, advection, and diffusivity. *J. Phys. Oceanogr.,* **30,** 201–214.

Paulson, C. A., and J. J. Simpson, 1977: Irradience measurements in the upper ocean. *J. Phys. Oceanogr.,* **7,** 952–956.

Qiu, B., 1995: Variability and energetics of the Kuroshio Extension and its recirculation gyre from the first two-year TOPEX data. *J. Phys. Oceanogr.,* **25,** 1827–1843.

——, 2000: Interannual variability of the Kuroshio Extension System and its impact on the wintertime SST field. *J. Phys. Oceanogr.,* **30,** 1486–1502.

——, and K. A. Kelly, 1993: Upper ocean heat balance in the Kuroshio Extension region. *J. Phys. Oceanogr.,* **23,** 2027–2041.

——, and W. Miao, 2000: Kuroshio path variations south of Japan: Bimodality as a self-sustained internal oscillation. *J. Phys. Oceanogr.,* **30,** 2124–2137.

——, K. A. Kelly, and T. M. Joyce, 1991: Mean flow and variability in the Kuroshio Extension from Geosat altimetry data. *J. Geophys. Res.,* **96,** 18 491–18 507.

Rahmstorf, S., 1993: A fast and complete convection scheme for ocean models. *Ocean Modelling,* **101** (unpublished manuscripts), 9–11.

Rao, S. S., 1989: *The Finite Element Method in Engineering.* Pergamon Press, 625 pp.

Renfrew, I. A., G. W. K. Moore, P. S. Guest, and K. Bumke, 2002: A comparison of surface-layer and surface turbulent-flux observations over the Labrador Sea with ECMWF analyses and NCEP reanalyses. *J. Phys. Oceanogr.,* **32,** 383–400.

Reynolds, R. W., and T. S. Smith, 1994: Improved global sea surface temperature analyses. *J. Climate,* **7,** 929–948.

Schmeits, M. J., and H. A. Dijkstra, 2001: Bimodal behavior of the Kuroshio and the Gulf Stream. *J. Phys. Oceanogr.,* **31,** 3435–3456.

Schneider, N., and A. J. Miller, 2001: Predicting western North Pacific Ocean climate. *J. Climate,* **14,** 3997–4002.

——, ——, and D. W. Pierce, 2002: Anatomy of North Pacific decadal variability. *J. Climate,* **15,** 586–605.

Scott, J. D., and M. A. Alexander, 1999: Net shortwave fluxes over the ocean. *J. Phys. Oceanogr.,* **29,** 3167–3174.

Smith, S. D., 1988: Coefficients for sea surface wind stress, heat flux, and wind profiles as a function of wind speed and temperature. *J. Geophys. Res.,* **93** (C12), 15 467–15 472.

Trenberth, K. E., and J. W. Hurrel, 1994: Decadal atmosphere–ocean variations in the Pacific. *Climate Dyn.,* **9,** 303–319.

Vigan, X., C. Provost, R. Bleck, and P. Courtier, 2000: Sea surface velocities from sea surface temperature image sequences, Part I: Method and validation using primitive equation model output. *J. Geophys. Res.,* **105,** 19 499–19 514.

Vivier, F., K. A. Kelly, and L. Thompson, 1999: Contributions of wind forcing, waves, and surface heating to sea surface height

observations in the Pacific Ocean. *J. Geophys. Res.*, **104,** 20 767–20 788.

Xie, S.-P., T. Kunitani, A. Kubokawa, M. Nonaka, and S. Hosoda, 2000: Interdecadal thermocline variability in the North Pacific for 1958–97: A GCM simulation. *J. Phys. Oceanogr.*, **30,** 2798–2813.

Zeng, X., M. Zhao, and R. E. Dickinson, 1998: Intercomparison of bulk aerodynamic algorithms for the computation of sea surface fluxes using TOGA COARE and TAO data. *J. Climate,* **11,** 2628–2644.

Zhang, Y. J., J. M. Wallace, and D. S. Battisti, 1997: ENSO-like interdecadal variability: 1900–93. *J. Climate,* **10,** 1004–1020.